A meso-scale model of clay matrix: the role of hydration transitions in geomechanical behavior

Farid Asadi, Hua-Xiang Zhu, Matthieu Vandamme, Jean-Noël Roux, Laurent Brochard

A meso-scale model of clay matrix: Role of hydration transitions in the geomechanical behavior

Farid ASADI[a], Hua-Xiang ZHU[b], Matthieu VANDAMME[a], Jean-Noël ROUX[a], and Laurent BROCHARD*[a]

While much progress has been made on the modeling of swelling clays at the molecular scale in the last decades, up-scaling to the macroscopic scale remains a challenge, in particular because the mesoscopic scale (between a few nanometers and a few hundreds of nanometers) is still poorly understood. In this article, we propose a new 2D granular model of clay addressing the mesoscale and adapted to the modeling of dense clay matrix relevant for geomechanics (up to pressures of 10-100 MPa). Some salient features of this model with respect to existing literature are 1- its ability to capture hydration transitions occurring at small basal spacing (essential to model the complex hydro-mechanical behavior such as drying shrinkage), 2- the flexibility of the clay layers that becomes important at pressures exceeding 1 MPa, and 3- the control of the inter-layer shear strength critical to model plasticity. The model calibration is purely bottom-up, based on molecular modeling results only. The case of Na-montmorillonite (Na-Mnt) is investigated in detail, regarding isotropic compression (elasticity and plasticity), yield surface and desiccation. The behavior of the granular model appears well consistent with what is known experimentally for pure Na-Mnt, and offers valuable insight into meso-scale processes that could not be reached so far (role of hydration transition, layer flexibility, impact of loading history). This granular model is a first step toward quantitative up-scaling of molecular modeling of swelling clay for geomechanical applications.

1 Introduction

Clay minerals are some of the most abundant geomaterials at the surface of the Earth and are involved in a wide variety of human activities. Clay-rich soils and rocks exhibit complex mechanical behaviors such as drying shrinkage, thermal contraction or salt sensitivity which has attracted a lot of attention in the engineering and scientific communities. Understanding and anticipating these complex behaviors is of central concern for many industrial and environmental applications from building foundations, to nuclear wastes storage and seismicity[1–3].

The elementary constituents of clay are nanometer-thin mineral layers, consisting of alternating silica tetrahedral sheets and metal oxide octahedral sheets. For instance, smectites combine an alumina octahedral sheet in between two silica tetrahedral sheets. Up to a few tens of such mineral layers pile up, with interstitial water between neighboring layers, to form stacks at the scale of about tens to hundreds of nanometers, which is often referred to as clay particle or stack. At the micrometer scale, the assembly of stacks form a matrix in which other mineral inclusions may be embedded (Fig. 1). The unusual macroscopic properties of clay are often attributed to the clay layer scale where electrostatic and steric interactions between the mineral and the inter-layer electrolyte (cations and bound water) generate a disjoining pressure. This excess pore pressure, and its sign, originates from the distribution of the ions and its dynamics (ionic correlation forces), as well as from the structure of the water surrounding the ions[4–6].

The magnitude of disjoining pressure is very sensitive to a variety of environmental factors (humidity, temperature, salt concentration, pH...) which causes the complexity of swelling clay behavior. For instance, drying shrinkage results from the change of disjoining pressure as humidity decreases[7–10]. Likewise irreversible thermal contraction is attributed to a decrease of maximum disjoining pressure leading to the drainage of confined water[11]. Other aspects of the macroscopic behavior are of more conventional origin, such as inter-stack pore water drainage during the primary consolidation of saturated clay[12–14]. Therefore, a physically-based modeling of clay-rich soils and rock requires a multi-scale description that takes into account the variety of relevant phenomena at the different scales, as schematically illustrated in Fig. 1.

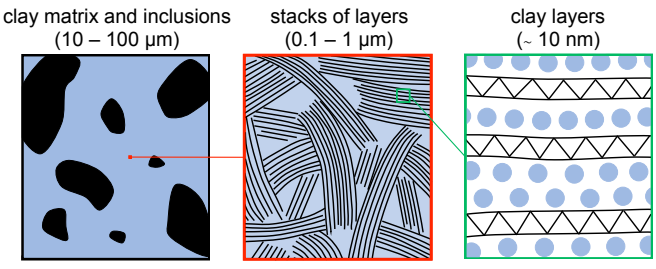

Fig. 1 Schematic description of the structural scale hierarchy of clay.

The nano-scale (Fig. 1 right) has long been studied in the literature both theoretically and experimentally. Clay layers are negatively charged while the confined fluid contains positive counterions. The classical description to such a system is based on

[a] Laboratoire Navier (UMR 8205), ENPC, Univ. Gustave Eiffel, CNRS, 6 & 8 avenue Blaise Pascal, 77455 Marne-la-Vallée, France. E-mail: laurent.brochard@enpc.fr
[b] Engineering Software Steyr, Berggasse 35, 4400 Steyr, Austria.

the theoretical framework of diffuse double layer (DDL) theory[15]. This theory considers a continuum representation of the solvent and counterions which is questionable when the inter-layer spacing corresponds to a few water molecules only (2 nm or less), which is the case of interest for clay in geomechanical conditions[8,10,16,17]. X-ray diffraction can provide the nano-scale structure of clay and points to the structuration of confined water in layers at small interlayer spacings (see for example[18–22]). Knowledge about the mechanics of the micro-scale relies mostly on molecular simulations techniques. Various molecular representations, from early idealized models to recent fully atomistic models, have been used to estimate the elementary mechanical behavior of clay layers and study the effect of humidity, temperature, nature of counterion etc.[7–9,23–26]. Recent molecular simulations are quite realistic and provide reasonable estimates of the elementary behavior at the layer scale[27–33]. In particular, one observes that the disjoining pressure is an oscillating function of the basal spacing, each decreasing branch corresponding to a (meta-)stable hydration state with an integer number of water layers. This is consistent with the structuration of confined water observed by X-ray diffraction. And, DDL theory cannot predict this oscillatory interaction since it neglects steric effects.

In contrast to the micro-scale, the meso-scale (Fig. 1 center) is poorly understood. Experiments at this scale are scarce because the mesoscale is too small for direct observation by microscopy and disorder makes it hard to interpret diffraction or scattering data[34]. Nevertheless some theoretical and numerical studies have investigated the meso-scale based on discrete element approaches. Early studies by Anandarajah[35,36] considered cluster of particles that are end-to-end bonded to form bendable mineral layers. The inter-layer interaction only considered the Electrostatic Repulsion (ER) through the Poisson-Boltzmann equation[37]. Additionally, Van der Waals Attraction (VdWA) was included in subsequent studies[36,38–42]. While ER and VdWA are medium/long-range interactions, the short-range response (Born's or steric repulsion) is generally treated by an elastic-frictional model[36,39–42]. These studies mostly focus on the isotropic and anisotropic compression behavior[35,36,39,41,42] and on the self-aggregation of mineral layers suspensions in water[40].

It is worth noting that almost all existing studies base their elementary potential (i.e., the inter-layer interaction) on the DDL framework such as the Derjaguin-Landau-Verwey-Overbeek (DLVO) theory[43], which is the consequence of the competition between ER and VdWA. As aforementioned, however, DDL is valid only at a relatively large inter-layer spacings, such as in colloidal suspensions, and is not valid at the inter-layer spacings of interest for geological conditions. In this respect, most existing granular models of the meso-scale are not suited to the study of dense systems corresponding to clay in geomechanical conditions. A valid description of the meso-scale should account for the peculiarity of the disjoining pressure at small inter-layer spacings. This is the case of very few meso-scale models so far. Ebrahimi et al.[44,45] do so to explore the meso-structure of an assembly of clay layers, by using the Gay-Berne potential[46] fitted against an interaction potential derived from fully atomistic simulations of a pair of clay layers. The free energy between two layers of Na-Montmorillonite (Na-Mnt) is obtained as function of the inter-layer spacing for different relative orientations of the layers. For parallel layers, which is the usual configuration for the study of disjoining pressure effects, two clear energy wells separated by an energy barrier form a W-shaped potential. This kind of multiple-well potential at small basal spacing (< 2 nm) is characteristic of the oscillatory disjoining pressure which reflects the structuration of the inter-layer hydration (i.e. the number of interstitial water layers). However, the Gay-Berne potential used by Ebrahimi et al., exhibits a single energy well, and therefore cannot capture hydration transitions of confined water.

In Discrete Element Methods (DEM), the clay layers are commonly modeled as simple rigid geometries, such as disks, platelets, or rigid ellipsoids for sake of simplicity and computational cost[34,43,47,48]. However, clay minerals exhibit very high aspect ratios: a layer is typically a nanometer thick and up to hundreds of nanometers long. Such high aspect ratios raise the question of the flexibility of the layer, which seems critical since highly bent microstructures are often observed[49,50]. In a recent work, we showed that flexibility might play a major role in the transition between hydration states by favoring wave-like propagation in front of the hydration transitions[51]. Very few granular modeling studies have addressed the issue of layer flexibility. Let us mention the early work of Anandarajah[35], who addressed flexibility by considering bendable mineral layers.

As for nanoscale hydration transitions, although this mechanism is at the heart of the peculiar hydro-mechanical behavior of clays[33], it has never been considered in existing granular models. Hydration transitions are thought to be involved in a variety of hydro-mechanical couplings of interest in geomechanics (drying shrinkage, thermal contraction, cation sensitivity). Hence the need for a meso-scale model that would take into account the multiple-well interaction between clay layers and the flexibity of the layer. Establishing such a model would pave the way for future investigations to relate the physics of nanometric clay layer to the macroscopic thermo-hydro-chemo-mechanical behavior. In this paper, we propose a new meso-scale modeling of the clay matrix, suited for dense system (i.e., geomechanical conditions) and able to capture the hydration transitions at the clay layer scale. The model is based on a W-shaped inter-layer potential combined with a flexible description of the clay layer. The model is fitted on atomistic simulations results from previous works (longitudinal and bending modulus of the layers, inter-layer oscillatory disjoining pressure, inter-layer shear and compressive strengths) and is implemented in 2D to investigate the role of hydration transition in the compressive behavior.

2 Materials and methods

2.1 Inter-layer interaction and w-potential

The meso-scale model we propose is a 2D system made of particles arranged to form chains, each chain representing a flexible hydrated clay layer. This section describes the inter-layer interaction which is at the heart of this model. Details about the construction of chain and intra-layer interactions are provided in the next section.

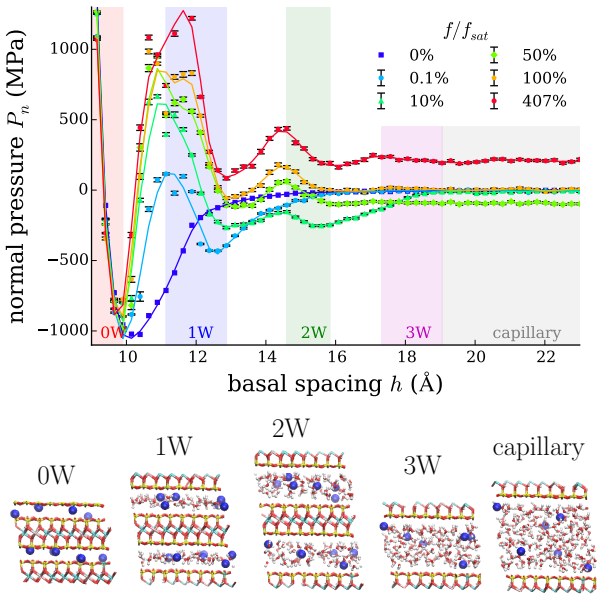

Fig. 2 Normal confining pressure P_n as a function of basal spacing h between two parallel layers of Na-Mnt in osmotic equilibrium with a water reservoir[33]. Several water fugacities relative to saturation (f/f_{sat}) are displayed, corresponding to equilibrium with bulk liquid ($f/f_{sat} \geq 100\%$) or bulk vapor ($f/f_{sat} \leq 100\%$, also known as relative humidity). The colored areas correspond to the average domains of basal spacings of the different hydration states xW (domains of decreasing pressure)[33].

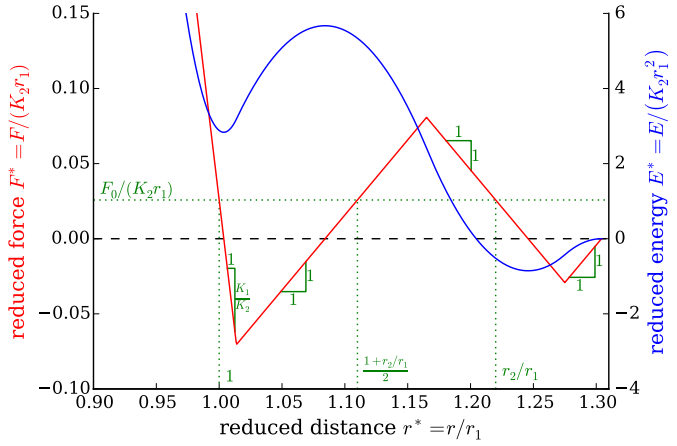

Fig. 3 Double well potential (w potential) used to model the inter-layer interactions. Normalized pair interaction force (red) and energy (blue) is represented as a function of the distance between two particles of different layers. We illustrate here the case of $F_0 > F_0^{eq}$ favoring the most hydrated state (F_0 is the additive constant on force, and F_0^{eq} is the the value of F_0 that ensures equal energy minima for the two wells).

Swelling clay contains 'adsorbed' or 'bound' water in between mineral layers that induces a normal confining pressure P_n between two hydrated clay minerals different from the usual pressure of the fluid (bulk pressure of an outside reservoir in osmotic equilibrium with the confined water). The difference between the two is called the disjoining pressure and is the mechanical force at the origin of the swelling at the layer scale. The integration of the confining pressure with respect to the basal spacing provides the effective interaction energy between hydrated clay layer that can serve for the calibration of a coarse-grained representation. Measuring the confining or disjoining pressures experimentally is very challenging, since it requires nanometric accuracy. It can be achieved with highly calibrated setups only (e.g., AFM). As an alternative to experiments, molecular simulation techniques provide reasonable estimates of the confining pressure and how it evolves with humidity or temperature. This is illustrated in Fig. 2 for a typical Na-montmorillonite model[33]. At small basal spacings (< 1 nm), the system reaches the solid-solid Born repulsion which is characterized by a sharp increase in confining pressure (dry '0W' state). Then, three oscillations of pressure are observed which reflect the presence of three hydration states at basal spacings around 1.2, 1.5, and 1.8 nm, respectively ('1W', '2W', and '3W' states). These pressure oscillations can be attributed to the ion distribution and water structuration within the inter-layer. Well-defined water density peaks corresponding to discrete water layers are observed. In the literature, these patterns are found commonly for swelling clays at small basal spacings[26]. The number and amplitude of the disjoining pressure oscillations depend on the nature of the clay, and are affected by the environmental conditions (humidity, nature of counterions, temperature). At larger basal spacings, other factors intervene such as salt concentration or pH. How disjoining pressure and hydration state are affected can explain, at least in part, some of the known macroscopic thermo-chemo-hydro-mechanical couplings of clay[11,18,22,26,31,33,52–54]. Usual geomechanical conditions correspond to basal spacings of less than 2 nm with one or two (possibly three) water layers. For the example of Fig. 2, the likely hydration transitions (change of number of water layers) are the 1W-2W transitions, which cover the range of pressure of most interest for geomechanical applications (up to a few hundreds MPa). The 0W state is expected to occur only in cases of extremely high pressures or extremely low relative humidity, while the 3W is expected only at high osmotic loading (fugacity) and remains limited to a narrow range of pressures. We disregard those two hydration states in this work, and the meso-scale model we propose hereafter focuses on the 1W-2W transitions only, considering the particular case of Na-Mnt (Fig. 2). But one can adapt the same model to any other particular case.

Inspired by the oscillatory confining pressure isotherm, we propose a mesoscale model of clay in which the inter-layer interaction follows a 'w-potential' reproducing the repulsive-attractive-repulsive interaction of the 1W - 2W domain of Na-Mnt. This potential is piecewise linear in force (F) and therefore exhibits two quadratic wells in energy (E). It applies to pairs of particles belonging to neighboring clay layers. The analytical formulations of the w-potential force and energy are given in Eq. 1 and 2, respectively; and displayed in a dimensionless form in Fig. 3. The force is made of five linear portions and is fully determined by five parameters: F_0 an additive constant to shift the force, r_1 and r_2 the equilibrium distances corresponding to $F = F_0$ (i.e., the position of energy minima for $F_0 = 0$), and K_1 and K_2 the two stiffnesses of the decreasing branches. The energy is obtained by integration of the force considering a zero energy at infinite distance.

$$F(r) =$$

$$\begin{cases} F_0 - K_1(r - r_1) & \text{if } r \leq \frac{\left(1+2\frac{K_1}{K_2}\right)r_1 + r_2}{2\left(1+\frac{K_1}{K_2}\right)} \\ F_0 + K_2\left(r - \frac{r_1+r_2}{2}\right) & \text{if } \frac{\left(1+2\frac{K_1}{K_2}\right)r_1 + r_2}{2\left(1+\frac{K_1}{K_2}\right)} \leq r \leq \frac{r_1+3r_2}{4} \\ F_0 - K_2(r - r_2) & \text{if } \frac{r_1+3r_2}{4} \leq r \leq \frac{5r_2-r_1}{4} \\ F_0 + K_2\left(r - \left(\frac{3r_2-r_1}{2}\right)\right) & \text{if } \frac{5r_2-r_1}{4} \leq r \leq \frac{F_0}{K_w} + \frac{3r_2-r_1}{2} \\ 0 & \text{if } \frac{F_0}{K_w} + \frac{3r_2-r_1}{2} \leq r \end{cases} \quad (1)$$

$$E(r) = \int_r^{+\infty} F(u)\,du =$$

$$\begin{cases} -F_0\left(r - \frac{3r_2-r_1}{2}\right) + \frac{K_1}{2}(r-r_1)^2 - K_1\frac{(r_2-r_1)^2}{8\left(1+\frac{K_1}{K_2}\right)} - \frac{(F_0)^2}{2K_2} \\ \qquad \text{if } r \leq \frac{\left(1+2\frac{K_1}{K_2}\right)r_1 + r_2}{2\left(1+\frac{K_1}{K_2}\right)} \\ -F_0\left(r - \frac{3r_2-r_1}{2}\right) - \frac{K_2}{2}\left(r - \frac{r_1+r_2}{2}\right)^2 - \frac{(F_0)^2}{2K_2} \\ \qquad \text{if } \frac{\left(1+2\frac{K_1}{K_2}\right)r_1 + r_2}{2\left(1+\frac{K_1}{K_2}\right)} \leq r \leq \frac{r_1+3r_2}{4} \\ -F_0\left(r - \frac{3r_2-r_1}{2}\right) + \frac{K_2}{2}(r-r_2)^2 - K_2\left(\frac{r_2-r_1}{4}\right)^2 - \frac{(F_0)^2}{2K_2} \\ \qquad \text{if } \frac{r_1+3r_2}{4} \leq r \leq \frac{5r_2-r_1}{4} \\ -F_0\left(r - \frac{3r_2-r_1}{2}\right) - \frac{K_2}{2}\left(r - \frac{3r_2-r_1}{2}\right)^2 - \frac{(F_0)^2}{2K_2} \\ \qquad \text{if } \frac{5r_2-r_1}{4} \leq r \leq -\frac{F_0}{K_2} + \frac{3r_2-r_1}{2} \\ 0 \qquad \text{if } -\frac{F_0}{K_2} + \frac{3r_2-r_1}{2} \leq r \end{cases} \quad (2)$$

The w-potential is a compromise between reflecting hydration transition (double well) and offering a simplistic representation. One can easily play on the parameters to mimic underlying couplings. For instance, the parameter F_0 controls the relative height of the two energy wells (Fig. 3), which is the driving mechanism of swelling and shrinkage upon humidity change[26]. Indeed, the difference of energy between the two wells is given by the integration of the force between r_1 and r_2. For a critical value $F_0 = F_0^{eq}$ (expression in Appendix A), the integration of the force cancels so that the wells are of equal energy. For $F_0 > F_0^{eq}$ the most hydrated state is favored which induces a swelling (case illustrated in Fig. 3). Conversely, for $F_0 < F_0^{eq}$ the least hydrated state is favored which induces a shrinkage. Thus, one can conveniently simulate the hydro-mechanical couplings arising from hydration transitions by acting on the value of F_0. Likewise, one could easily simulate the effects of counterions exchange or temperature change by acting on the energy barrier ΔE between the two wells[11] (expression in Appendix A).

For numerical implementation, we rather use a dimensionless formulation of the potential, so that we are left with three independent parameters only. The dimensionless formulation we used is detailed in Appendix B. Nevertheless, in what follows we refer to quantities with dimension, since the mesoscale model is calibrated on molecular simulation results and confronted to laboratory data.

2.2 Clay layer description

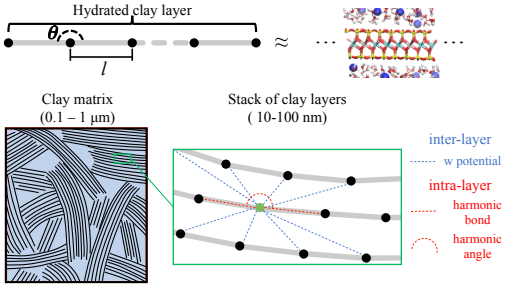

Fig. 4 Schematic representation of the 2D mesoscale model. Chains of particles represent flexible hydrated clay layers. Intra-layer energy is modeled by nearest neighbors interactions with harmonic bonds and angles. Inter-layer energy is modeled by the double well pair potential (Fig. 3) capturing the 1W and 2W hydration states.

Our mesoscale model of clay is based on a description of each mineral layer as a flexible linear chain of N particles as shown schematically in Fig. 4. The inter-layer interaction (i.e., the interaction between particles in different layers) is given by the w-potential presented in the previous section. The intra-layer interactions are made of $(N-1)$ harmonic bonds between neighboring particles and $(N-2)$ harmonic angles between neighboring bonds. Doing so, the chain exhibits longitudinal and bending stiffnesses in response to a mechanical loading. The expressions of the elongation and bending potentials are:

$$\begin{cases} E_{angle}(\theta) = K_{angle}(\theta - \theta_0)^2 \\ E_{bond}(l) = K_{bond}(l - l_0)^2 \end{cases}, \quad (3)$$

where K_{angle} and K_{bond} are the bending and elongation moduli, respectively; θ and l are the angle between neighboring bonds and bond length, respectively; and the subscript $_0$ refers to the equilibrium angle or length. How the intra-layer moduli K_{angle} and K_{bond} are derived from the mechanical properties of the mineral layers (longitudinal and bending stiffnesses) is explained in the Appendix C.

Describing the clay layer with many particles is quite expensive computationally in comparison with granular models considering single non-spherical particles to represent a clay layer (e.g., the model of Ebrahimi et al.[44] based on the Gay-Berne potential). Nevertheless, such a description makes it possible to simulate more complex meso-structures with staggered and distorted arrangements of layers, whereas single particle layers are limited to ideally arranged and rigid stacks. Based on simple scaling estimates, one can show that flexibility and disorder are expected to play a major role in the mechanics of the clay matrix[51]. The proposed model can adapt to the wide variety of possible meso-structures that can arise from the material genesis (sedimentation process, condition of deposition, biological processes, etc.) and

loading history.

For confrontation with experiments, one has to estimate what is the porosity (or void ratio) of an assembly of such particles, that is to say, one has to define the solid thickness t of a layer. The usual laboratory measurement of the void ratio consists in drying a sample at low relative humidity or high temperature, and measuring the solid volume that remains. Doing so, the thickness of the layer corresponds to the basal spacing of the hydration state prevailing at the low humidity/high temperature, which is not necessarily the 0W state depending on the nature of the clay. For instance, at 300K and 20% relative humidity, K-Mnt is mostly in the 0W state, Li-Mnt in the 1W state, and Mg-Mnt in the 2W state[54] (X-Mnt refers to the montmorillonite with element X as counterion). For the case considered here (sodium Wyoming montmorillonite), the dry state is the 1W state, which is valid for relative humidities down to about 10%[33]. Accordingly, we considered r_1 (thickness of the 1W state) as the thickness of the layer. In what follows, all estimates of porosity and void ratios assume a layer thickness of r_1.

Regarding the conversion from 2D to 3D, we assume translational invariance in the third dimension. To convert pressures and energies from 2D to 3D, We consider a length l_0 of the clay layers in this third dimension. The 3D results are independent of this particular choice, since initial calibration is in 3D.

2.3 Model calibration

The parameters of the model are calibrated based on the results of full atomic simulations. The inter-layer w-potential is a particle-particle interaction but does not represent the layer-layer behavior directly, because each particle of a given chain interacts with several particles of a neighboring chain (Fig. 4). In this respect, the intra-layer distance l_0 and the cutoff are expected to play an important role in the layer-layer interaction. While the w-potential is designed to reproduce the normal layer-layer behavior, it also controls the shear behavior, and, again, l_0 will appear critical. Overall, the parameters of the model should be determined so as to ensure that the total interaction between adjacent layers fits the layer-layer behavior estimated from full-atomic simulation. The piece of information that is the most well known about the layer-layer behavior is the normal confining pressure isotherm, which captures the normal mechanical response at zero shear (Fig. 2). The confining pressure isotherm brings no information about the shear behavior. Much less is known about the shear behavior, and, in this work, we considered the shear strength ($\sim$ 2 to 20 MPa) estimated by Carrier[30] from creep shear tests in full-atomic molecular dynamic simulations.

When two clay layers are facing each other, each particle of a layer interacts with a few particles of the other layer. We represent in Fig. 5 the ideal case of two parallel infinite layers (a periodic cell is displayed only), where the relative position of the two layers is described by the basal spacing h and the shear displacement s as defined on the Figure. This configuration of two layers is ideal since it corresponds to an infinite system under uniform loading at its boundaries, i.e., stress and deformation are uniform over the length of a layer (no bending, no elongation). This is of particular interest for the calibration of the model, since it corresponds to the conditions of the full-atomic simulations to estimate the confining pressure and shear strength. The energy landscape obtained after the calibration explained below is displayed with a colormap in Fig. 5.

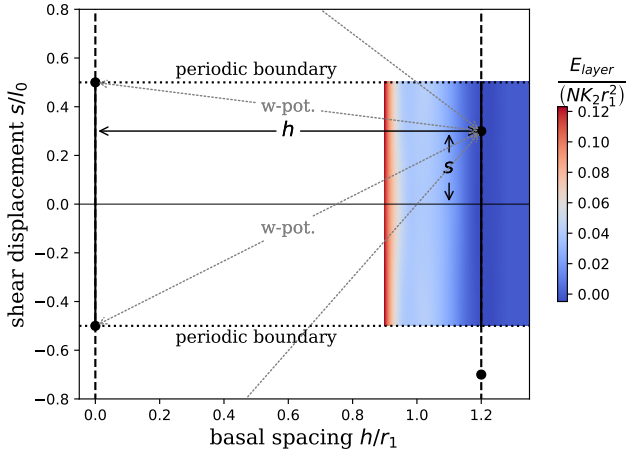

Fig. 5 Schematic diagram of a periodic portion of two adjacent parallel layers showing the inter-particle interactions involved.

The calibrated inter-layer potential is displayed by 2D and 3D charts in Fig. 6. To avoid confusion, one should clearly note that the w-potential displayed in Fig. 3 represents a single interaction between a pair of particles and is for illustration only (parameters are not calibrated). Whereas, Fig. 6 represents the interaction between two parallel layers (i.e., sum of many pairs of particles) and considers the calibrated parameters.

By construction the potential exhibits some variations with the shear displacement s, which reflects the discrete nature of the meso-scale representation. Although the effect of s is hardly visible on Figs. 5 and 6, it does affect the convexity of the potential. The magnitude of the variations with s is mostly controlled by the distance l_0 between particles in a chain: the higher l_0, the higher the variations. These variations provide some shear strength to the layer-layer interaction and also some variability in the normal mechanical response. The confining pressure isotherms correspond to the normal layer-layer interaction under zero shear stress, that is for $s = 0$ or $s = \pm l_0/2$. The model is calibrated against the isotherm of Fig. 2 corresponding to a relative fugacity of 1, i.e., a relative humidity of 100%. The 2D normal pressure is computed by differentiating with respect to h the layer-layer energy per unit length of the chain. To convert the 2D pressure to 3D, we consider a length of l_0 in the third dimension. We do so for all energy contributions (elongation, bending, and w-potential) which ensures consistency (any other value than l_0 would be suitable as long as the same is considered for all the contributions). Therefore, the equivalent 3D normal pressure of the layer-layer interaction is given by:

$$P_n = -\frac{1}{Nl_0^2}\left.\frac{\partial E_{layer}}{\partial h}\right|_s \tag{4}$$

where the convention considered is $P_n > 0$ in compression and

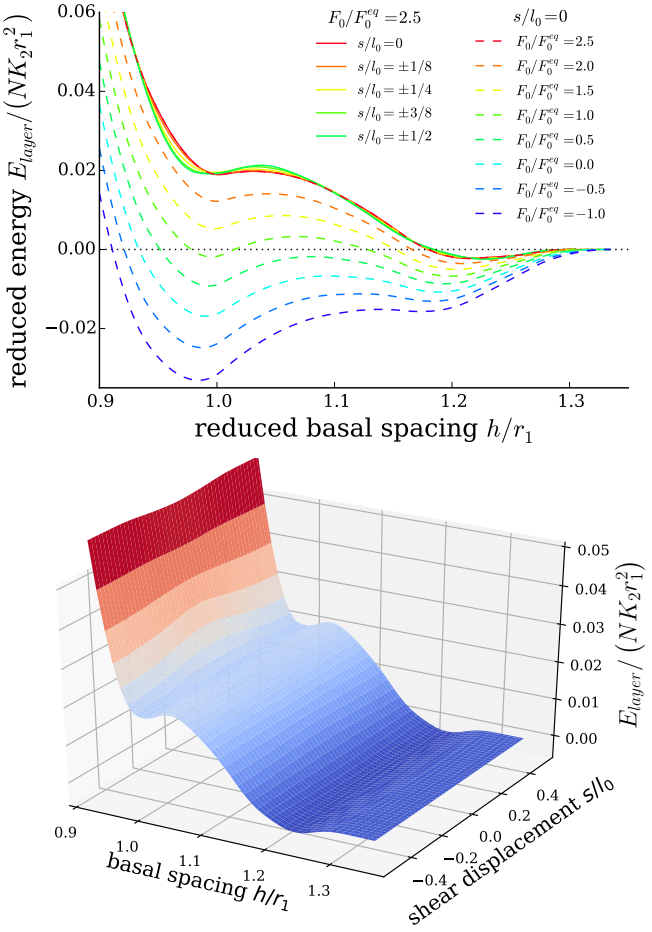

Fig. 6 2D and 3D charts (top and bottom respectively) of the layer-layer interaction energy in function of the basal spacing h and shear displacement s.

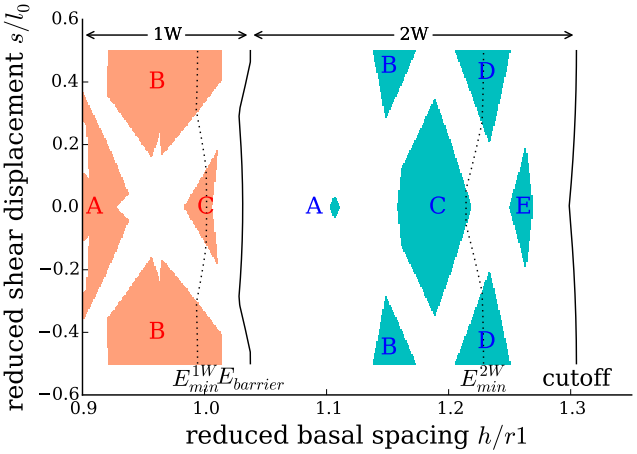

Fig. 7 Domains of stability of the layer-layer interaction, i.e., domains where the Hessian matrix has positive eigenvalues only. Various disconnected domains can be identified within each hydration state. By symmetry, some domains appear twice and we use the same label in such cases. E_{min}^{1W} and E_{min}^{2W} represent the positions of the 1W and 2W energy minima, respectively. $E_{barrier}$ represents the position of the energy maximum between the two wells. And 'cutoff' represents the position where the energy reaches zero.

$P_n < 0$ in traction.

Regarding the constraint on shear strength, we first compute the shear stress of the layer-layer interaction by differentiation of the energy per unit chain length with respect to the shear displacement s and converting it to 3D:

$$P_s = -\frac{1}{Nl_0^2}\left.\frac{\partial E_{layer}}{\partial s}\right|_h \tag{5}$$

We then compute the full yield surface of the layer-layer interaction (from pure normal stress to pure shear stress). Note however, that there are several yield surfaces, since one must distinguish the hydration states (1W and 2W), but also the various domains of stability of these hydration states. Under stress control, the layer-layer interaction is stable if the Hessian matrix of the interaction energy has positive eigenvalues only. Owing to the roughness of the energy map, it appears that there are several disconnected domains of stability for both the 1W and the 2W hydration states (see Fig. 7). The yield surface is given by the stress states at the boundary of those stability domains, so there are as many yield surfaces as stability domains. The overall domain of admissible stresses for each hydration state is the union of the admissible domains of the different stability regions, and the overall yield surface is the boundary of this admissible domain. A notable difference between the two hydration states is that the 2W state exhibits a moderate compressive strength corresponding to the hydration transition, whereas the 1W state exhibits a compressive strength orders of magnitude higher and of unphysical nature (one layer snaps through the other). The compressive strength of the 1W state should never occur in practical implementation of the model unless extreme compression is applied to the system. In this work, we investigate compressive stresses that do not exceed a few hundreds MPa which correspond to loadings

of interest in geomechanics. Accordingly, we disregard the 1W compressive strength. The computation of the yield surfaces is used to fit the shear strength of the clay layer.

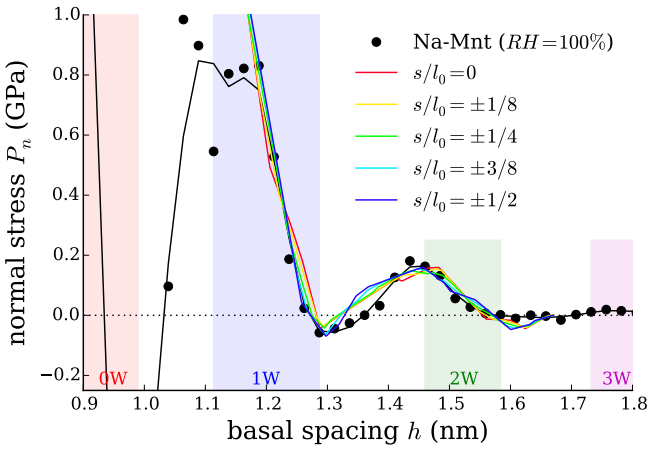

Fig. 8 Normal pressure P_n between two layers fitted on the confining pressure isotherm of Na-Mnt at 100% relative humidity and 300K[33]. The normal pressure is given for different shear displacements s, but only the cases $s=0$ and $s=l_0/2$ do correspond to a zero shear stress as is the case of the full-atomic simulations. The black line is a Savitzky-Golay filter to smoothen the raw molecular simulation data. The changes of slopes in the inter-layer pressure is reminiscent of the piecewise linear force associated with the w-potential (Fig. 3).

The calibration of the model consists in a combined fit of the shear strength and of the 1W-2W portion of the confining pressure isotherm. This calibration is non trivial since many properties are targeted at the same time, and we proceed by a first rough calibration treating the normal and shear behavior separately, to determine approximate values of the intra-layer distance and w-potential parameters. The calibration is then refined by considering all aspects together over a few iterations. The fit we propose is shown in Fig. 8 for the confining pressure and Fig. 9 for the yield surface. The corresponding set of parameters is listed in Table 1. The calibrated model corresponds to a layer-layer interaction that favors the 2W hydration state (minimum energy lower for 2W than for 1W). This is indeed the case at high relative humidity[33] or beyond saturation[32]. As relative humidity is reduced below 60%, the isotherms tend to favor the 1W state instead, leading to the drying shrinkage[33]. In this work, we initially calibrated the model to represent a high humidity situation, but the effect of a drying or heating triggering a transition from the 2W to the 1W state is investigated, by modulating the value of F_0 (see section 3.5). Regarding the shear strength, the fit is necessarily inaccurate since one cannot control separately the shear strengths of the two hydration states. We obtain a shear strength of about 22 MPa for the 1W state and 6 MPa for the 2W state, while the estimations of Carrier[30] are 14-19 MPa and 1-3 MPa, respectively. The calibrated values overestimate the molecular simulations results, but the calibrated shear strengths remain an order of magnitude smaller than the tensile/compression strengths, so that the fitting in shear is highly sensitive in absolute value but remains acceptable relative to the accuracy with respect to the normal behavior. Reaching such a high contrast between shear and normal strengths requires rather small values of the intra-layer distance ($l_0/r_1=0.25$), so that the roughness of the potential in the shear direction is much smaller than the evolution with basal spacing (Fig. 3).

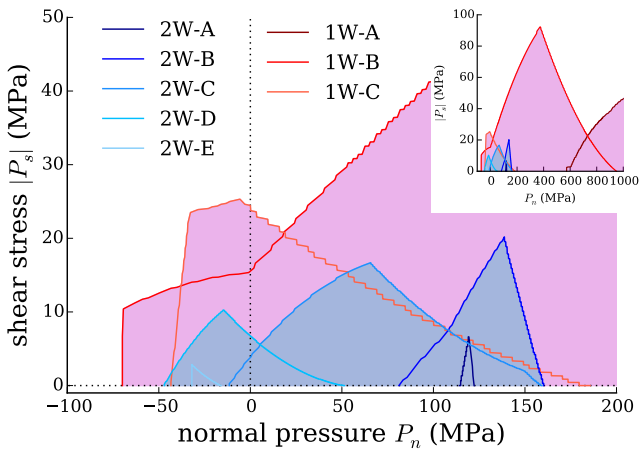

Fig. 9 Yield surface of the two hydration states, obtained by combining the yield surface of the various stability domains in Fig. 7. The inset displays the yield surface at higher pressure and shear stresses. The '1W-A' domain corresponds to rather high compression and is visible only in the inset. The model is calibrated so that the strength in pure shear ($P_n=0$) approaches the range estimated by Carrier[30] (from 1-3 MPa for the 2W the state to 14-19 MPa for the 1W state).

With this calibration, a single particle inside a chain represents approximately a mass of matter of $m\approx 3\cdot 10^{-25}$ kg. This estimate is approximate since a particle represents a variable amount of matter depending on the hydration state (1W or 2W), i.e., on the inter-layer distance.

Table 1 Calibrated parameters of the meso-scale model

K_2 (N/m)	r_1 (nm)	l_0/r_1	K_1/K_2
0.06	1.28	0.25	7
$(r_2-r_1)/r_1$	$F_0/(K_2 r_1)$	$K_{angle}/(K_2 r_1^2)^\sharp$	$K_{bond}/K_2^\sharp$
0.22	0.025283143	610	4000
	($\Leftrightarrow F_0=2.5F_0^{eq}$)	61	400

$^\sharp$ For K_{angle} and K_{bond}, the largest value is the one estimated from the layer elasticity (appendix C). The lowest value is the one considered for most of the simulations (see motivation in section 2.4). Sensibility to K_{angle} and K_{bond} is investigated in section 3.4.

This granular model is implemented in the LAMMPS software (https://www.lammps.org/)[55], and all calculation in this paper, except post-processing, are done with this software. Velocity-Verlet integration and Langevin thermostat[56] are used to simulate Brownian dynamics at controlled temperature. For pressure-controlled simulations, a Berendsen barostat[57] is used.

2.4 Preparing initial meso-structures

As mentioned in the introduction, the structure of the clay matrix at the meso-scale (10 nm to 100 μm) is poorly known. In particular, while stacks of clay layers (particles) are expected in order

to reach low porosity arrangements, how large these particles are is debated. In this respect, we propose hereafter a procedure to generate meso-scale arrangements with desired degree of stacking. This procedure makes it possible to control the extent of clay particles. In the absence of clear knowledge about the actual extent of clay particles, several meso-structures with various degrees of stacking are generated and investigated in this work.

First of all, a starting configuration is prepared in a 2D periodic domain containing a 20×20 square lattice. Chains of particles of different lengths are introduced at each lattice site with random orientations. Five chain lengths are considered corresponding to 20, 30, 40, 50, and 60 particles, i.e., clay layers from 6.4 nm to 19.2 nm. When introducing the chains in the 2D lattice, the chain length is chosen randomly among those 5 lengths. The lattice size ($164 \cdot l_0$) is chosen to ensure no overlap between the chains. An example of starting configuration is shown in Fig. 10. Such a system contains about 16k particles, arranged as a suspension of 400 chains in a 2D volume of 1049.6×1049.6 nm^2. The chosen chain lengths correspond to the low range of what is usually suggested in the literature [58,59] (from 10 nm to a few μm). In this study, we favored small chain lengths in order to limit the computational cost. All the systems studied here can be reasonably simulated with a few CPUs and do not require high performance computers. We acknowledge that considering rather small chain lengths might introduce some bias in the model. In particular, under a uniform load, the magnitude of intra-layer bending is expected to scale as the cube of the length, whereas the displacement associated with the inter-layer interaction is expected to scale linearly with the length. Otherwise said, considering small chain length is expected to bias the meso-scale model by favoring less layer bending than with longer chains. To limit this bias, we reduced the bending and elongation moduli (K_{angle} and K_{bond}) by one order of magnitude (Tab. 1) in order to make the layers more flexible and thus compensate for the small length of the layers. The impact of modifying K_{angle} and K_{bond} is investigated specifically in section 3.4.

Then, an isotropic compression at constant engineering strain rate is applied to the starting configuration during a temperature-controlled Langevin dynamics. This compression brings the system to a 2D volume of 136×136 nm^2, corresponding to a void ratio of 1.8 and a pressure close to the ambient pressure (10^5 Pa). The Brownian motion combined with the compression produces stacks of clay layers. The choice of temperature and loading rate strongly influence the degree of stacking observed at the end of the compression: more stacks are formed as temperature is increased and loading rate is decreased. We choose a reduced temperature of $\frac{k_b T}{K_2 r_1^2} = 0.004$ which remains small compared to the energy barrier of the w-potential (Fig. 6, $\frac{\Delta E_{layer}}{N K_2 r_1^2} \approx 0.02$), so that it does not trigger any 2W-1W transitions. Several reduced engineering volumetric strain rates $\dot{\varepsilon}_v^* = \dot{\varepsilon}_v \sqrt{m/K_2}$ are considered from $-1.9 \cdot 10^{-6}$ to $-2.8 \cdot 10^{-4}$, leading to very different degrees of stacking (Fig. 10). Considering the approximate mass of a particle, these simulations correspond to actual time scales up to a few μs, i.e., much larger than what can be achieved by usual molecular dynamics, but still small in comparison with usual laboratory time scales.

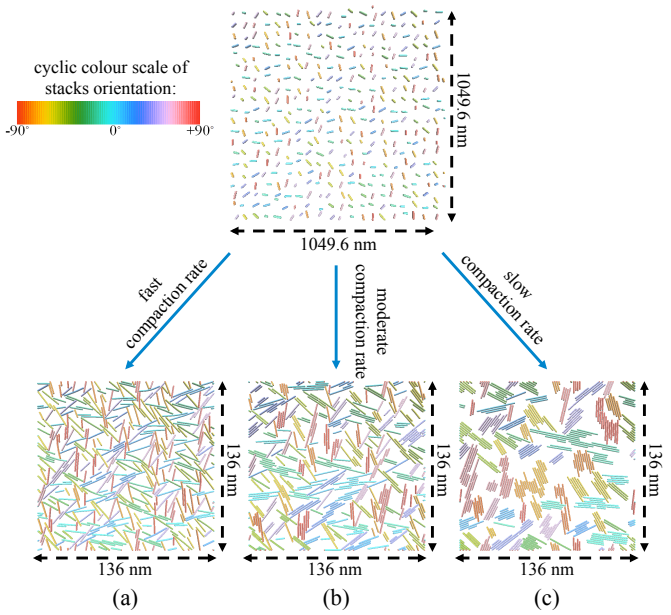

Fig. 10 System configurations obtained after isotropic compression of the initial suspension: (a) fast compaction rate ($\dot{\varepsilon}_v^* = -2.8 \cdot 10^{-4}$), (b) moderate compaction rate ($\dot{\varepsilon}_v^* = -1.9 \cdot 10^{-5}$), (c) slow compaction rate ($\dot{\varepsilon}_v^* = -1.9 \cdot 10^{-6}$). The particles are colored based on the orientation of their chain, thus highlighting the stacks of layers sharing the same local orientation.

As it can be seen in Fig. 10, one can control the degree of stacking through the compaction rate. A quantitative indicator of the degree of stacking is the inter-layer energy per particle. The case of two parallel infinite chains in the 2W hydration state (second well in Fig. 6) provides the minimum inter-layer energy one can reach for a system in which all the layers would form a single periodic stack ('fully-stacked meso-structure'): $\frac{E_{layer}}{N K_2 r_1^2} = -0.0068$. One expects the inter-layer energy to decrease linearly from 0 to this limit value as the number of pairs of stacked layers increases. We display in Fig. 11 the obtained inter-layer energy as a function of the compaction time (in log scale). The shortest compaction time correspond to the fast compaction in Fig. 10, and the longest compaction time to the slow compaction. Interestingly, the inter-layer energy per atom decreases linearly with the logarithm of the compaction time, and this linear trend appears in line with the theoretical limit of a fully-stacked meso-structure. This suggests that the proposed approach is able to generate any degree of stacking by choosing the appropriate compaction time. Since the time dependence is logarithmic in Fig. 11, reaching high stacking is computationally expensive (488h of CPU time for the longest compaction time considered here). The proposed method is interesting because it is very simple and it relies on a single control parameter (compaction rate). Of course, there are more efficient ways to generate stacking. One can consider alternative algorithm. One can also consider coarsening the layer discretization for the preparation procedure since intra-layer bending and inter-layer sliding remain negligible (however, considering the precisely calibrated discretization becomes essential for further

mechanical characterization).

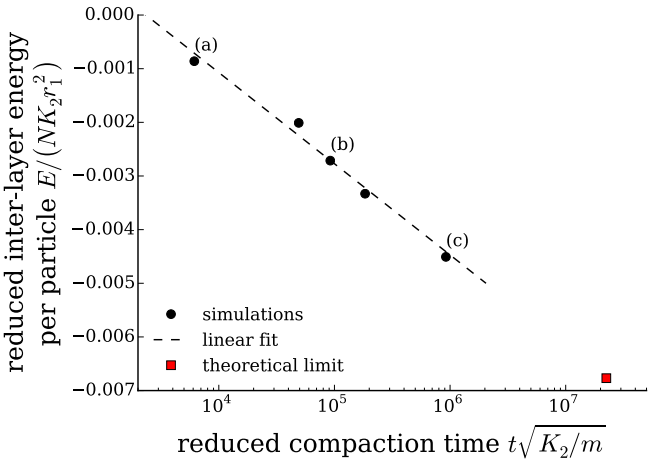

Fig. 11 Inter-layer energy per particle as a function of the compaction time (in log scale). The red point corresponds to the extrapolation of the linear trend to the theoretical limit corresponding to the inter-layer energy of a fully-stacked meso-structure. The systems (a), (b), and (c) are those of Fig. 10.

In the next section, we propose a detailed investigation of the meso-scale model considering the three meso-structures of Fig. 10. More precisely, we characterize the local anisotropy and the hydration state, and investigate the elastic and plastic mechanical behavior, as well as the response to osmotic loading (drying). The overall relevance of the bottom-up approach is challenged by confronting those predictions with typical experimental data for clays.

3 Results and discussions

3.1 Local anisotropy due to stacking

The stacking of clay layers causes a local anisotropy since the layers in a stack share the same orientation. This local anisotropy is readily visible in Fig. 10. A classical characterization of anisotropy is based on the nematic order parameter Q[34,60] which we adapt here for a 2D system: for each particle i, with chain normal axis $\left(u_i^x, u_i^y\right)$, we define an order two tensor $\mathbf{Q_i}$ as follows:

$$Q_i^{kl} = 2u_i^k u_i^l - \delta^{kl} \tag{6}$$

where $(k,l) \in \{x,y\}$ are the 2D Cartesian axis, and $\delta^{kl} = 1$ if $k = l$ and 0 otherwise. The per-particle tensor is averaged over all particles in a volume to obtain a tensor order parameter $\mathbf{Q} = \langle \mathbf{Q_i} \rangle$, which is traceless symmetric. The two opposite eigenvalues $\pm Q$ (nematic order parameter) characterize the anisotropy within the volume: if the system is highly ordered (anisotropic), Q approaches 1, and if the system is disordered (isotropic), Q is close to zero.

For each of the meso-structures of Fig. 10, we characterize the order parameter for both the total volume and local sub-volumes by dividing the simulation cell into equal sub-cells. We display in Fig. 12 the average Q over all sub-cells of same volume, and represent it as a function of the linear size of the sub-cells. For the largest size corresponding to the total volume, all the three systems are mostly isotropic with Q values of about 0.1. Q is expected to vanish in the limit of infinite sizes. The observed values are non negligible, suggesting minor anisotropy, which we attribute to the small size of the system. One can guess that reaching negligible anisotropy of the systems would require significantly larger systems, with typically 5 to 10 times more particles. Reaching such system size is computationally demanding and would require to improve first the computational efficiency.

As smaller volumes are considered, the average Q increases significantly with values greater than 0.5 for all systems for sub-cells of 10 nm, characterizing the local order due to the clay layers at this scale. One readily observes a clear hierarchy between the three meso-structures: the average Q is larger when there is more stacking (i.e., as the compaction rate used is slower).

TEM images of Na-Mnt available in the literature[61–63] exhibit significantly longer clay layers than considered in our model. As discussed in section 2.4, considering short layers is necessary to limit the computational cost. The stacking, however, is quite consistent with TEM observations for Na-Mnt[61,62]: through a detailed analysis of the meso-structures, one finds that the average number of layers in a stack is 2.1 ± 0.6 for system (a), 4.1 ± 2.2 for system (b), and 5.7 ± 3.3 for system (c). System (c) seems to be the most consistent with respect to existing small-angle X-ray scattering data for Na-montmorillonite[61] (8 layers at ambient pressure, note that this is particularly small compared to other types of clay). Yet, one cannot fully discard the less stacked arrangements (a and b) since scattering or high resolution microscopy mostly highlight ordered domains. Accordingly, in what follows, we will consider all three meso-structures equally representative of realistic clay systems.

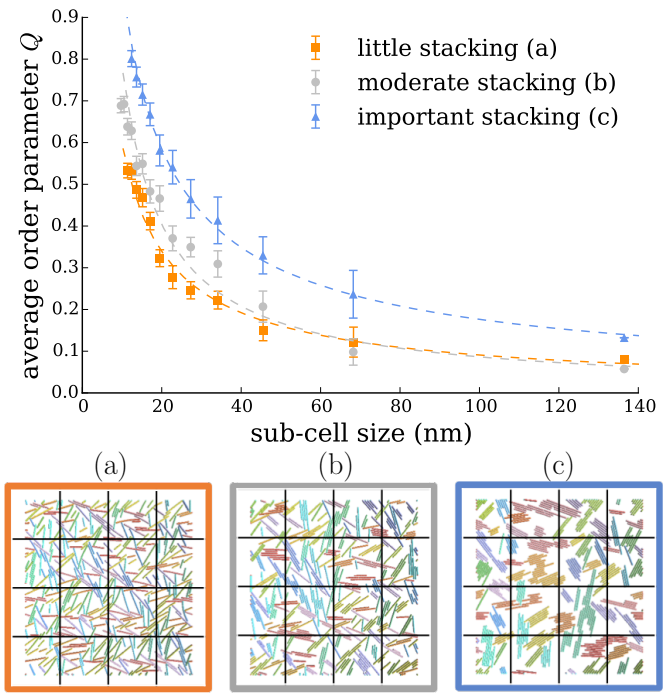

Fig. 12 Local nematic order parameter Q as a function of the sub-cell size for the three meso-structures of Fig. 10. The largest size corresponds to the entire volume. Sub-cells are obtained by dividing the total volume into equal sub-cells (see schematic example at the bottom when divided into 4 by 4).

3.2 Isotropic compression

Let us now investigate the mechanical behavior. The three meso-structures ((a), (b), and (c) in Fig. 10) are subjected to isotropic compression at constant engineering volumetric strain rate ($\dot{\varepsilon}_v^* = \dot{\varepsilon}_v\sqrt{m/K_2} = 6.52\cdot10^{-5}$). The mechanical response depends on the considered strain rate (see Fig. 20 in appendix D), and we make sure to use the same strain rate for all the simulation. The investigation of rate effects is left for future studies. As before, the system evolution is simulated with a Langevin dynamics but at a much lower temperature ($\frac{k_bT}{K_2r_1^2} = 2.0\cdot10^{-8}$), so that thermal agitation becomes negligible. To assess the importance of the initial meso-structure, the isotropic compression is performed on 15 different meso-structures (5 of type (a), 5 (b), and 5 (c)), for which the initial suspension in the preparation procedure is systematically different (section 2.4).

We display in Fig. 13 the relationship between void ratio e and pressure P. Each curve represents one degree of stacking ((a), (b), or (c)), and corresponds to the average curve of the corresponding 5 meso-structures. The standard deviation associated with the variability in mechanical response between the 5 meso-structures is shown by the shaded domains. The variability for each degree of stacking is moderate, suggesting good repeatability of these results. One readily observes a logarithmic response in pressure ($e = e_0 + C_c\log(P/P_0)$), as is generally observed for clay-rich soils[64]. No data for Na-Mnt at these high pressures could be found in the litterature, but we can confront the simulation results to experimental data reported by Baille et al. [65] for 10 specimens of normally consolidated bentonite (more than 60% of Mnt), with various levels of compaction. The meso-scale model falls in the good range, although some deviation is observed at large pressure which can be attributed to the fact that the bentonite is not 100% Mnt contains mostly divalent counter-ions (Ca, Mg) which strongly limits the dehydration, while it contributes significantly to compressibility for Na-Mnt (see next section).

In the domain of moderate loadings ($P \leq 1$ MPa), the predicted compression index ($C_c = \partial e/\partial(\log P) = 0.9\pm0.05$) and reference pressure ($P_0 = 0.8\pm0.1$ MPa for $e_0 = 1$) are quite consistent with experimental results of oedometer tests available in the literature for pure montmorillonite[66] ($C_c = 0.92$, and $P_0 = 2$ MPa for $e_0 = 1$). While the compression index C_c is well predicted, the reference pressure P_0 is somehow underestimated. We can attribute this discrepancy to the fact that the simulations are 2D, and to the absence of long range electrostatic repulsion in our model. At higher loadings ($P \geq 1$ MPa), the slope of the compression curve evolves toward smaller compression index ($C_c = 0.45\pm0.05$). No experimental data could be found for pure montmorillonite in this domain of pressure, but oedometer tests on bentonite[65] (mostly montmorillonite) confirm that a smaller compression index is expected above 1 MPa with values between 0.32 and 0.53.

As can be seen in Fig. 13, increasing the degree of stacking (from (a) to (c)) tends to shift the mechanical response to lower pressures, with little impact of the compression index. More precisely, at a given void ratio $P_{(a)} \approx P_{(b)} \approx 1.35P_{(c)}$, except at very high compression ($e < 0.5$, $P > 5$ MPa). Interestingly, at such high compression the pressure shift vanishes and the mechanical responses become almost identical when approaching $e = 0.4$ and $P = 10$ MPa. Looking at the corresponding meso-structures after compression (Fig. 13 bottom), they appear relatively similar, suggesting that under high pressure (here 10 MPa), the system has lost memory of its initial meso-structure and the mechanical response becomes independent of the initial degree of stacking. The initial meso-structure seems to influence the mechanical response at moderate compression only ($P < 0.4$ MPa). A detailed analysis of the compressed meso-structures reveals that there remains some differences in the number of layers in a stack: 9.7 ± 6.0 for system (a), 8.7 ± 4.6 for system (b), and 15.3 ± 10.2 for system (c). The stacking of system (c) is more consistent with experimental estimates for compressed Na-montmorillonite[61] (15 layers at 1 MPa, 20 layers at 100 MPa), suggesting meso-structure (c) is the most representative.

3.3 Hydration States

A specificity of the proposed meso-scale model is the ability to capture hydration state at the layer scale. In this section, we investigate the hydration states of the meso-structures and follow their evolution during the isotropic compression. The formal limits of the hydration states in terms of basal spacings have been calculated in Fig. 7. Accordingly, to determine the hydration state of a particle, we use the minimum distance between this particle and that of the neighboring chains. Based on these distances, a particle is found to be either in the 1W state (closer than the energy barrier), or in the 2W state (between the energy barrier and the cutoff), or in the suspension (beyond the cutoff). Follow-

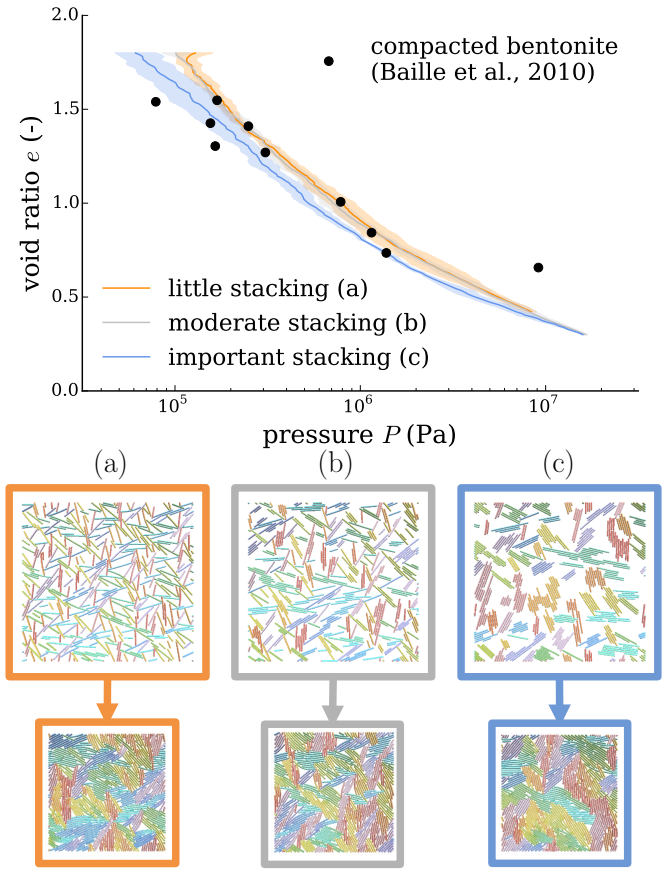

Fig. 13 Mechanical response of the meso-scale model under isotropic compression. The three curves correspond to the three degrees of meso-structure stacking (Fig. 10). Five different meso-structures are considered for each degree of stacking and the curves presented are averages. The standard deviations are represented by the shaded areas. Snapshots of meso-structures before and after compression are displayed at the bottom. The simulation results are confronted to experimental data reported by Baille et al. [65] for 10 specimens of normally consolidated bentonite, with various levels of compaction.

ing this methodology, we report in Fig. 14 the hydration states of the three meso-structures ((a), (b), and (c)), before and after the isotropic compression.

Before compression, we observe significant differences in hydration states between the three meso-structures. The proportion of 2W state increases a lot with the degree of stacking. Let us recall that the 2W state is the most favorable state in terms of energy (Fig. 3), and is the state which is expected in stacks of layers at moderate pressures. It is thus expected that the meso-structures with more stacks exhibit more 2W states. Apart from the 2W state, the majority of the remaining layers are in the suspension state before compression, i.e., are not facing another layer. Interestingly, a non negligible proportion of 1W state is found in the least stacked meso-structure (a), whereas this hydration state is energetically much less favorable than the 2W and suspension states. Detailed analysis of the snapshots shows that these 1W states are mostly located at the edge of the layers where there is a high propensity to force concentrations triggering the 2W-1W transition.

After compression, the distributions of hydration states have changed a lot. No more suspension is found, and a very significant portion of the layers are now in the 1W state in all three meso-structures. The significant proportion of 1W is remarkable considering the fact that the pressure barrier to trigger the 2W-1W transition for ideally parallel layers (110 MPa in Fig.8), is much larger than the average confining pressure reached at the end of the isotropic compression (16 MPa). This suggests that the heterogeneity of the meso-structures leads to large stress concentrations with local stresses up to one order of magnitude larger than the average stress. It is worth noting also that the increase in proportion of 1W are very similar when comparing the meso-structures (+29% for (a), +32% for (b), and +27% for (c)). In other words, the compression has triggered the same amount of 2W-1W transitions in all three systems, suggesting little impact of the initial meso-structure on the 1W-2W transition. Detailed analysis of the evolution during compression shows that most of the 2W-1W transitions have occurred under high compression ($e < 0.5$, $P > 5$ MPa) at a stage where the meso-structures are very similar, hence the little dependence to the initial meso-structure. Also, the 1W states that were already present before compression appear to be very stable and are preserved until the end of the compression. Since the 2W-1W transition is associated with a large irreversible deformation ($(r_1 - r_2)/r_1 = -22\%$) at the layer scale, it causes an apparent plastic deformation at the meso-scale. While the primary origin of plasticity is generally attributed to the fabric evolution (porosity, stacking, layer sliding), we identify here a plastic phenomenon of 'osmotic' origin (hydration transition). Although hydration transition accounts for only a small fraction to the total plastic deformation (about 10-15% of the total compaction between 1 MPa and 10 MPa), it is essential to explain some peculiar thermo-hydro-mechanical couplings of swelling clays, for instance the irreversible thermal compaction during drained heating [11]. We provide here the first meso-scale model that would be able to address quantitatively such peculiar couplings.

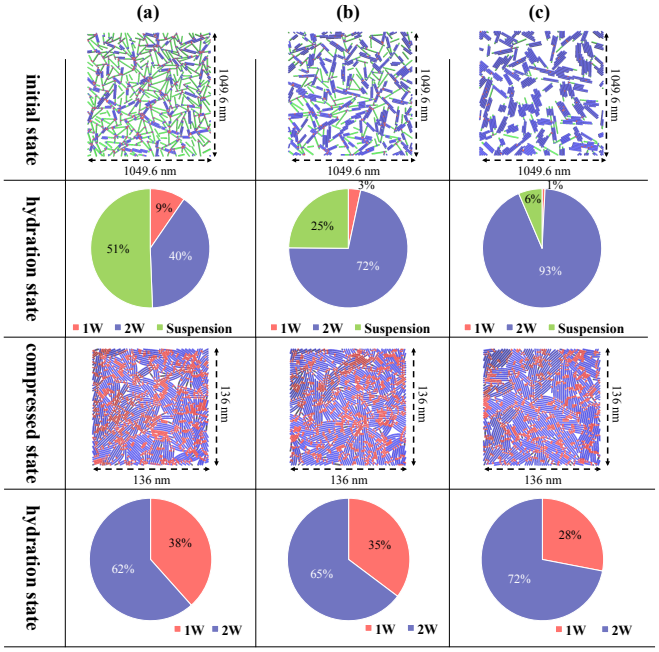

Fig. 14 Hydration states of the three mesostructures (a), (b), and (c) of Fig. 10 before and after compression. The pie charts represent the respective proportions of the hydration states : 1W, 2W and suspension.

3.4 Role of layer flexibility

As explained in section 2.4, we deliberately considered lower intra-layer stiffnesses (K_{bond} and K_{angle}) to limit the bias due to the small chain lengths. In this section, we assess the sensibility of the isotropic compression behavior to the choice of intra-layer stiffnesses. We investigate both the elastic and plastic behaviors by performing additional re-compression test at intermediate void ratio. Starting from the meso-structure (c) (high degree of stacking in Fig. 10), an isotropic compression is simulated as in Fig. 13, but an additional de-compression and re-compression loop is performed at a void ratio of 0.9. Two situations are compared: one with the original values of K_{bond} and K_{angle} (called 'stiff layer'), and one with the reduced values (called 'flexible layer'), as provided in Tab. 1. The two mechanical responses are compared in Fig. 15.

We observe that the layer stiffness increases the ratio $C = \partial e/\partial(\log P)$ of the elastic and plastic behaviors. The impact on the plastic response is somehow moderate, with a compression index (C_c) that changes by 25 % from 0.41 for the stiff layer to 0.51 for the flexible layer. In comparison, the inter-layer moduli were varied by one order of magnitude. Accordingly, the plastic behaviors appear little affected by the layer stiffness. Interestingly, the difference in plastic moduli vanishes at low void ratios ($e < 0.6$), suggesting that the role of layer bending in the plastic response becomes negligible for highly compacted systems. Regarding the elastic behavior, the impact of the layer flexibility is much more more significant: the re-compression index (C_r) increases five fold from 0.01 for the stiff layer to 0.05 for the flexible layer. Such a difference is comparable to the change prescribed to the inter-layer moduli K_{bond} and K_{angle}, suggesting that layer bending and stretching are some of the main mechanisms controlling the elastic behavior. Interestingly, experimental estimate of the re-compression index for pure montmorillonite[66] ($C_r \approx 0.1$) are more consistent with the value obtained for the flexible layer, which support our choice to consider deliberately lower values of K_{bond} and K_{angle} to compensate for the small length of the layers. In fact, the high sensibility of the re-compression index to the layer stiffness could be considered as a way to calibrate the choice of K_{bond} and K_{angle} when the length of the layers is chosen not representative to limit computational cost.

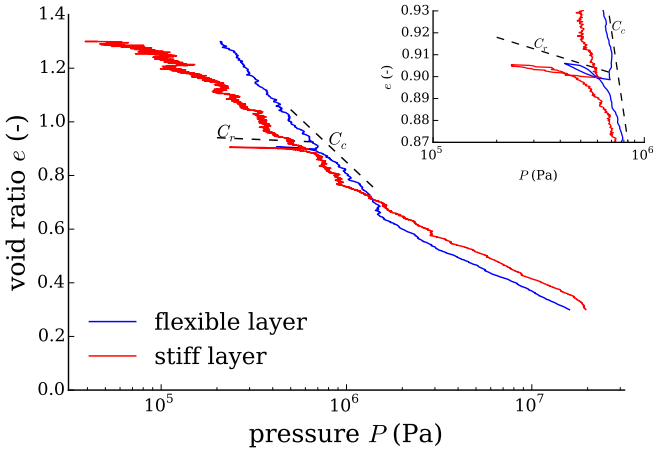

Fig. 15 Comparison of the isotropic compression curves for the reference parameterization of layer stiffness ($K_{bond}/K_2 = 4000$, $K_{angle}/(K_2 r_1^2) = 610$, stiff layer) and for the modified parameterization ($K_{bond}/K_2 = 400$, $K_{angle}/(K_2 r_1^2) = 61$, flexible layer). The dashed lines represent the local slope corresponding to the compression index C_c (plastic branch), and to the re-compression index C_r (elastic branch).

3.5 Desiccation and re-hydration

The proposed meso-scale model is designed to capture the hydration transition at the layer scale. Varying the reference force F_0, one can mimic an osmotic loading during which the most favorable hydration state is changed (Fig. 6 top). In practice such change of hydration state is triggered by changes of relative humidity or temperature. Low humidity and high temperatures favor desiccation, whereas high humidity and low temperature favor re-hydration. In this section, we apply osmotic loadings via F_0 to investigate the response to desiccation and re-hydration. This simulation of the osmotic loading is quite rudimentary, and an accurate modeling such as reproducing in detail the behavior of Fig. 2 would require more complex formulations of the inter-layer potential and modifying multiple parameters at the same time. This is left for future studies.

The consolidation state is known to strongly influence the response to osmotic loadings[11], so two consolidation states are investigated: a normally consolidated state, and an over-consolidated state. Both configurations are prepared starting from the meso-structure (c) (Fig. 10). The normally consolidated state is obtained by isotropic compression at a void ratio of $e = 0.8$ ($P = 1$ MPa). The over-consolidated state follows the same compression, but the system is then unloaded at a pressure of $P = 0.1$ MPa (Fig. 16). The two configurations are then submitted to a

desiccation by decreasing the value of F_0 from $2.5F_0^{eq}$ (reference value) to $-F_0^{eq}$. The corresponding evolution of the inter-layer interaction is displayed in Fig. 6. Through this evolution, the relative position of the 1W and 2W energy levels are reversed, starting in favor of 2W, and finishing in favor of 1W. Ten increments of F_0 are considered to simulate a progressive osmotic loading, while the pressure on the system is maintained constant by a Berendsen barostat. At each loading step the system is equilibrated for a reduced time of $t\sqrt{K_2/m} = 6.14 \cdot 10^3$ so that is reaches a stationary volume. We also investigate the reversibility of the osmotic response by performing re-hydration. Similarly, ten increments of F_0 are considered to vary it from $-F_0^{eq}$ to $2.5F_0^{eq}$ at constant pressure. The evolution of the void ratio over the desiccation / re-hydration cycle is displayed in Fig. 17 (top). We also display the evolution of the porosity by evaluating the porosity accessible to the center of probe particle as a function of the probe particle radius (Fig. 17 bottom). After desiccation or re-hydration, we re-investigate the isotropic compression behavior until 100 MPa. All the loading paths are displayed in Fig. 16.

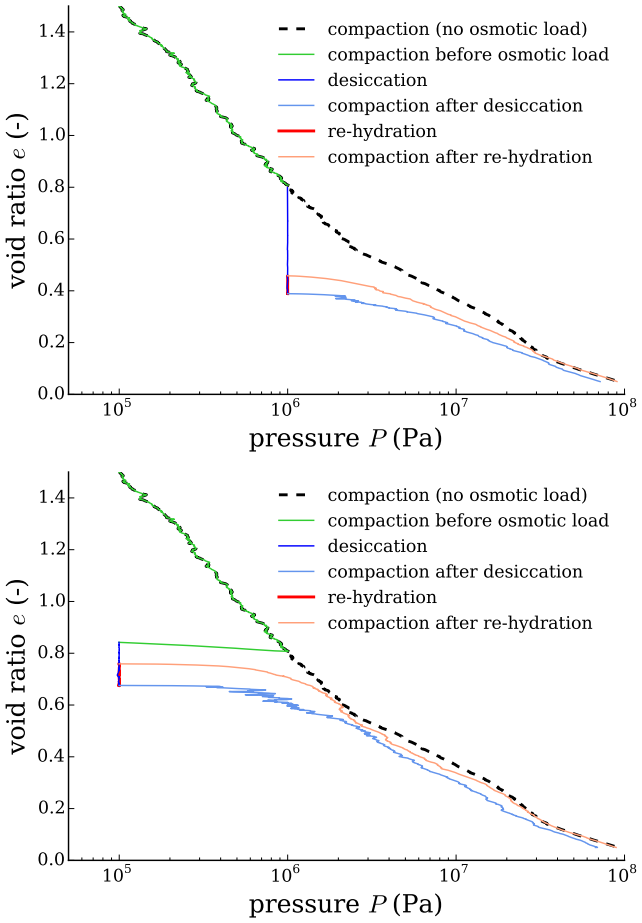

Fig. 16 Evolution in the P-e diagram of the normally consolidated (top) and over-consolidated (bottom) systems during the desiccation / re-hydration process.

One readily observes that the magnitude of the shrinkage is much larger for the normally consolidated configuration than for the over-consolidated model (Fig. 17 top). The magnitude of

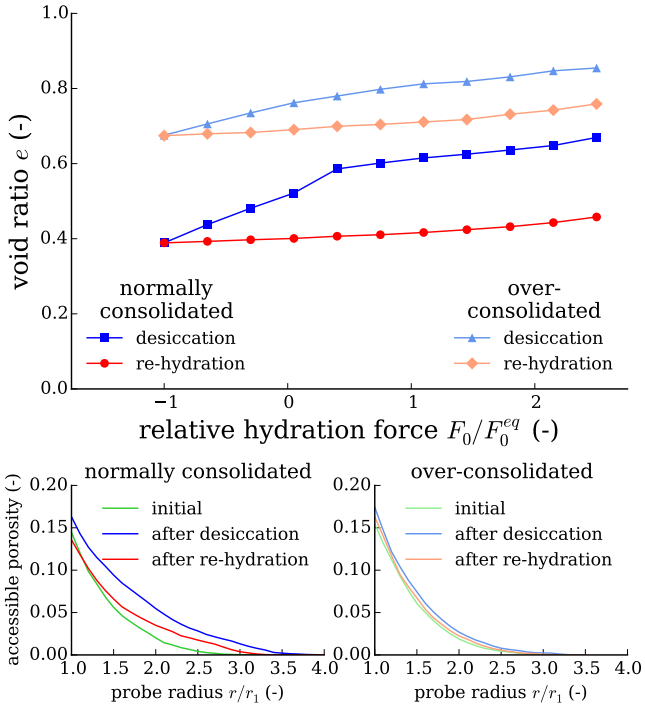

Fig. 17 (top) Void ratio of the normally consolidated and over-consolidated systems during the desiccation / re-hydration cycle. (bottom) Porosity accessible to the center of a probe particle as a function of the probe particle radius. The different curves show the evolution during the osmotic loading.

shrinkage during desiccation for the normally consolidated configuration (-17%) is comparable to the magnitude of the layer scale deformation upon 1W-2W transition ($(r_1 - r_2)/r_2 = -0.18$). Most of the 2W layers have change hydration state and become 1W. Yet, the deformation is not uniform, because, while the mineral layers contract, the porosity increases (Fig. 17 bottom). This is attributed to the interlocking of the meso-structure because mineral contraction is anisotropic. For the over-consolidated systel, the smaller shrinkage (-9%) is due to an incomplete 2W-1W transition (only about half of the 2W layers), while the porosity increase is also much smaller. Therefore, the loading history (normally consolidated vs. over-consolidated) has a major impact on the osmotic behavior. Differences in the meso-structures between normally and over-consolidated systems are barely visible with the naked eye, but the underlying distribution of stresses and strains is strongly affected, which causes the difference in osmotic behavior. This highlights the critical role of the meso-structure in the upscaling of clay properties. The effect of over-consolidation on the magnitude of drying shrinkage is consistent with experimental observations for clayey materials[67]: shrinkage of normally consolidated materials is 2 to 3 times larger than shrinkage of over-consolidated materials. While deformations of tens of % are frequent for pure montmorillonite[68], geomaterials with significant fractions of swelling clay generally exhibit much smaller macroscopic shrinkage than what could be expected from the shrinkage of their clay fraction with simple mixture rules, and the same is observed for cement which shrinks much less than

what could expect from the shrinkage of its calcium silicate hydrates with simple mixture rules[69]. A possible explanation is of course the presence of other non swelling mineral inclusions, and how they affect strain localization. But we show here that, even without non-swelling inclusions, the meso-structure can exhibit much smaller deformation than the nano-layers (here depending on the loading history).

The magnitude of re-swelling is relatively the same in the re-hydration process, irrespective of the consolidation state. Approximately half of the shrinkage is recovered during re-hydration for the over-consolidated state, whereas less than one fourth is recovered for the normally consolidated case. And the change in porosity is also only partly recovered. Actually, analysis of the meso-structure shows that much less 1W-2W transitions occur during re-hydration, than 2W-1W transitions during desiccation. The irreversibility of re-swelling is consistent with experimental observations for clayey materials[67]: less than half of the shrinkage is recovered, irrespective of the consolidation state. Interestingly, the link between consolidation state and irreversibility echoes what is observed in drained heating experiments[11]: normally consolidated clays exhibit much larger irreversible compaction than over-consolidated clays, and the reversible deformation recovered during cooling is mostly independent from the consolidation state. While this phenomenon was long attributed to the hydration transitions at the layer scale, existing theory remains qualitative. The proposed meso-scale model opens the door to quantitative estimations.

Re-compaction after osmotic loading approaches the original plastic behavior but the more 2W-1W transitions occurred during osmotic loading the longer it takes to reach the original plastic curve. Therefore, the over-consolidated system after re-hydration (least 2W-1W transitions) is the fastest one to reaches the original plastic behavior, while the normally consolidated system after desiccation (most 3W-1W transitions) is the slowest one. This can be explained by the fact that the plastic behavior is recovered when the hydration states are similar, so when pure compaction has triggered enough hydration transition compared to the osmotic loading.

3.6 Yield surface

So far, we investigated the response to isotropic loading only. In this section, we consider anisotropic loadings and focus more specifically on the yield surface. To determine the yield surface, the meso-structure (c) is first prepared in an over-consolidated state (same procedure as in the previous section: isotropic compression up to 1 MPa, followed by isotropic unloading to 0.1 MPa). This over-consolidated state is then submitted to different anisotropic loadings, from purely spherical to purely deviatoric. The determination of the yield surface is difficult, since the transition from elasticity to plasticity is actually progressive. For sake of simplicity, we opted for a basic rule: the yield point during a loading is the onset of the first 'major' drop in deviatoric stress q (small local drops are neglected). This rule applies well to most of the loading curves except in 3 cases when the loading is almost spherical (i.e., q remains small). In that case, yield is detected as the first major extremum of pressure (maximum in compression, minimum in tension). We display in Fig. 18 the estimated yield surface (dots). The obtained surface exhibits a distinctive elliptic shape, which is consistent with the usual plasticity models of clay[13]. On the tension side, a moderate cohesion of about $c = 50$ kPa is observed, which is quite typical for clays[64]. Interestingly, this cohesion remains much smaller than the shear and tension strength at the nano-scale (about 10^4 kPa), hence a major role of the meso-structure. Although a particular yield surface always depends on the loading history (pre-consolidation pressure), the friction angle at the point of maximum deviatoric stress ($\Phi = \arctan\left((q-C)/p\right)$) is usually considered as independent of this history, and characterizes the clay plastic behavior. The friction angle obtained here ($\Phi = 14°$) is again in the typical range for clays[64], but somehow higher than expected for pure Na-Mnt ($8°$)[70]. Overall, this yield surface appears reasonably consistent with usual clay behavior. Yet, in the perspective of future studies, larger system sizes would be worth investigating to assess the size effects, improve the initial isotropy and reduce the noise of the results.

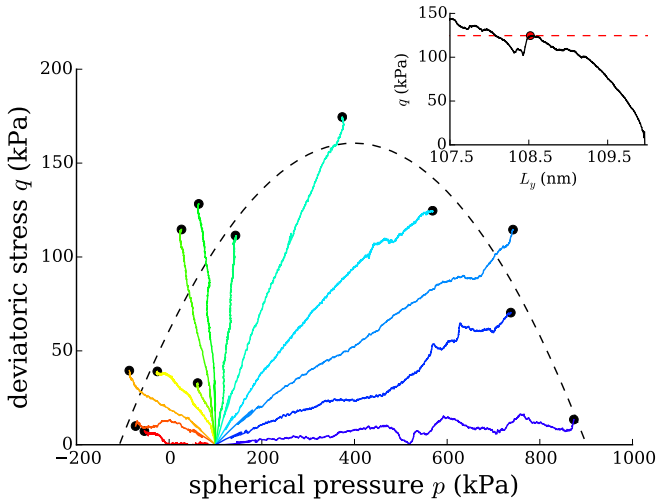

Fig. 18 Yield surface for a system initially consolidated at 1 MPa and unloaded at 0.1 MPa (isotropic compression). Several loading directions are probed (plain lines). The point of yielding (dots) are detected at the onset of a major drop in deviatoric stress (see example of uniaxial compression in inset), except close to pure compression (violet) or pure traction (red and orange) for which yielding corresponds to a local maximum of pressure, or minimum of pressure, respectively. An approximate yield surface is displayed by the dashed line.

4 Conclusions

In this paper, we proposed a new 2D granular model of swelling clay at the mesoscale that addresses specifically the issue of dense assemblies of clay layers, representative of geomechanical conditions. This model is built to reproduce the inter-layer mechanics at small basal spacing (xW states), and the intra-layer flexibility that becomes significant at pressures exceeding a few MPa. The formulation of the model makes it possible to simulate not only mechanical loadings but also osmotic loadings through the inter-layer potential that captures the effect of humidity of tempera-

ture changes. The model is purely bottom-up since it is calibrated on molecular simulation results. The particular case of Na-Mnt is considered, and the predictions of the granular modeled are successfully confronted to known experimental behaviors of Na-Mnt. Thus, this granular model paves the way to quantitative up-scaling of molecular models of swelling clays. It also provides valuable insight into the processes occurring at the mesoscale that were inaccessible so far, notably:

- How hydration states are distributed within the meso-structures and how they contribute to the thermo-hydro-mechanical behavior.
- How layer flexibility affects the elastic and plastic behaviors at larges pressures.
- How clay layers are locally arranged in stacks, and how it affects the mechanics.
- How loading history relates to stress distribution at the mesoscale, which strongly affects the osmotic behavior.

We believe this work opens interesting perspectives with respect to the fundamental understanding of swelling clays, and it shall motivate further studies on the mesoscale of clays.

The two main limitations of the current model are 1) the fact that it is 2D, and 2) the system and layers sizes which remain small. Both limitations were constrained by the computational cost, but significant computational improvements are possible by opting for alternative aggregation algorithms (the preparation procedure is the most expansive part), and by coarsening the layer discretization when layer flexibility is unnecessary ($P < 1$ MPa) or by homogenizing layers within large stacks. Such improvements would make it possible to consider 3D systems and / or much larger systems in the future. Transposition of this work to 3D can follow a similar route regarding elaboration and calibration of the potential, but one will have to specify the extension of the layer in the third dimension, which may be quite irregular[58].

5 Acknowledgment

Funding from the ALLUVIUM project is gratefully acknowledged. The ALLUVIUM project is part of the FUTURE consortium and is funded in the framework of the Programme Investissement d'Avenir supervised by the French National Research Agency (ANR). We also acknowledge support from the VARAPE and ARPENTONS projects, which are part of the NEEDS/MIPOR initiative (CNRS, ANDRA, CEA, EDF, IRSN, BRGM).

Notes and references

1 L. D. Jones and I. F. Jefferson, in ICE manual of geotechnical engineering: Volume I, 2012, vol. 7, pp. 413–441.

2 Andra, Evaluation of the feasibility of a geological repository in an argillaceous formation, Agence nationale pour la gestion des déchets radioactifs Technical Report December, 2005.

3 F. M. Chester, C. Rowe, K. Ujiie, J. Kirkpatrick, C. Regalla, F. Remitti, J. C. Moore, V. Toy, M. Wolfson-Schwehr, S. Bose, J. Kameda, J. J. Mori, E. E. Brodsky, N. Eguchi and S. Toczko, Science, 2013, **342**, 1208–1211.

4 R. J. Pellenq, J. M. Caillol and A. Delville, The Journal of Physical Chemistry B, 1997, **101**, 8584–8594.

5 K. Ioannidou, B. Carrier, M. Vandamme and R. Pellenq, EPJ Web of Conferences, 2017, **140**, 01009.

6 F. Dragulet, A. Goyal, K. Ioannidou, R. J.-M. Pellenq and E. Del Gado, The Journal of Physical Chemistry B, 2022, **126**, 4977–4989.

7 E. S. Boek, P. V. Coveney and N. T. Skipper, Langmuir, 1995, **11**, 4629–4631.

8 E. J. M. Hensen and B. Smit, The Journal of Physical Chemistry B, 2002, **106**, 12664–12667.

9 T. J. Tambach, E. J. M. Hensen and B. Smit, The Journal of Physical Chemistry B, 2004, **108**, 7586–7596.

10 R. Anderson, I. Ratcliffe, H. Greenwell, P. Williams, S. Cliffe and P. Coveney, Earth-Science Reviews, 2010, **98**, 201–216.

11 L. Brochard, T. Honório, M. Vandamme, M. Bornert and M. Peigney, Acta Geotechnica, 2017, **12**, 1261–1279.

12 M. A. Biot, Journal of Applied Physics, 1941, **12**, 155–164.

13 A. N. Schofield and P. Wroth, Critical state soil mechanics, McGraw-hill London, 1968, vol. 310.

14 B. M. Das, Advanced Soil Mechanics, CRC Press, 2013.

15 W. B. Russel, D. A. Saville and W. R. Schowalter, Colloidal Dispersions, Cambridge University Press, 1989.

16 M. Boström, D. R. M. Williams and B. W. Ninham, Physical Review Letters, 2001, **87**, 168103.

17 H. Bayesteh and A. Hoseini, Computers and Geotechnics, 2021, **130**, 103913.

18 R. W. Mooney, A. G. Keenan and L. A. Wood, Journal of the American Chemical Society, 1952, **74**, 1371–1374.

19 Crystal Structures of Clay Minerals and their X-Ray Identification, ed. G. W. Brindley and G. Brown, Mineralogical Society of Great Britain and Ireland, 1980.

20 E. Ruiz-Hitzky and A. Van Meerbeek, in Developments in Clay Science, 2006, pp. 583–621.

21 M. Smalley, Clay Swelling and Colloid Stability, CRC Press, 2006.

22 E. Ferrage, B. Lanson, L. J. Michot and J.-L. Robert, The Journal of Physical Chemistry C, 2010, **114**, 4515–4526.

23 J. P. Valleau, R. Ivkov and G. M. Torrie, The Journal of Chemical Physics, 1991, **95**, 520–532.

24 R. T. Cygan, J.-J. Liang and A. G. Kalinichev, The Journal of Physical Chemistry B, 2004, **108**, 1255–1266.

25 T. J. Tambach, P. G. Bolhuis and B. Smit, Angewandte Chemie International Edition, 2004, **43**, 2650–2652.

26 T. J. Tambach, P. G. Bolhuis, E. J. M. Hensen and B. Smit, Langmuir, 2006, **22**, 1223–1234.

27 R. Shahsavari, M. J. Buehler, R. J. Pellenq and F.-J. Ulm, Journal of the American Ceramic Society, 2009, **92**, 2323–2330.

28 R. Shahsavari, R. J. Pellenq and F.-J. Ulm, Phys. Chem. Chem. Phys., 2011, **13**, 1002–1011.

29 Y. Zheng, A. Zaoui and I. Shahrour, Applied Clay Science, 2011, **51**, 177–181.

30 B. Carrier, Ph.D. thesis, Université Paris Est, 2013.
31 E. Ferrage, Clays and Clay Minerals, 2016, **64**, 348–373.
32 T. Honorio, L. Brochard and M. Vandamme, Langmuir, 2017, **33**, 12766–12776.
33 L. Brochard, The Journal of Physical Chemistry C, 2021, **125**, 15527–15543.
34 E. Ferrage, F. Hubert, E. Tertre, A. Delville, L. J. Michot and P. Levitz, Physical Review E, 2015, **91**, 062210.
35 A. Anandarajah, Journal of Geotechnical Engineering, 1994, **120**, 1593–1613.
36 A. Anandarajah, Géotechnique, 2000, **50**, 509–519.
37 E. J. W. Verwey and J. T. G. Overbeek, Theory of the Stability of Lyophobic Colloids, Elsevier Publishing Company, inc., 1948.
38 S. Kutter, J.-P. Hansen, M. Sprik and E. Boek, The Journal of Chemical Physics, 2000, **112**, 311–322.
39 M. Yao and A. Anandarajah, Journal of Engineering Mechanics, 2003, **129**, 585–596.
40 N. Lu, M. T. Anderson, W. J. Likos and G. W. Mustoe, International Journal for Numerical and Analytical Methods in Geomechanics, 2008, **32**, 965–980.
41 K. J. Sjoblom, Journal of Geotechnical and Geoenvironmental Engineering, 2016, **142**, 06015013.
42 A. G. Pagano, A. Tarantino, M. Pedrotti, V. Magnanimo, K. Windows-Yule and T. Weinhart, EPJ Web of Conferences, 2017, **140**, 15023.
43 S. Bandera, C. O'Sullivan, P. Tangney and S. Angioletti-Uberti, Computers and Geotechnics, 2021, **138**, 104333.
44 D. Ebrahimi, A. J. Whittle and R. J.-M. Pellenq, The Journal of Chemical Physics, 2014, **140**, 154309.
45 D. Ebrahimi, A. Whittle and R.-M. Pellenq, Clays and Clay Minerals, 2016, **64**, 425–437.
46 J. G. Gay and B. J. Berne, The Journal of Chemical Physics, 1981, **74**, 3316–3319.
47 D. R. Katti, M. I. Matar, K. S. Katti and P. M. Amarasinghe, KSCE Journal of Civil Engineering, 2009, **13**, 243–255.
48 D. Ebrahimi, R. J. Pellenq and A. J. Whittle, Granular Matter, 2016, **18**, 49.
49 Y.-T. Fu, G. D. Zartman, M. Yoonessi, L. F. Drummy and H. Heinz, The Journal of Physical Chemistry C, 2011, **115**, 22292–22300.
50 D. Tunega and A. Zaoui, The Journal of Physical Chemistry C, 2020, **124**, 7432–7440.
51 T. Honorio, L. Brochard, M. Vandamme and A. Lebée, Soft Matter, 2018, **14**, 7354–7367.
52 N. Wada, D. R. Hines and S. P. Ahrenkiel, Physical Review B, 1990, **41**, 12895–12901.
53 G. J. da Silva, J. O. Fossum, E. DiMasi and K. J. Måløy, Physical Review B, 2003, **67**, 094114.
54 E. Ferrage, B. Lanson, N. Malikova, A. Plançon, B. A. Sakharov and V. A. Drits, Chemistry of Materials, 2005, **17**, 3499–3512.
55 A. P. Thompson, H. M. Aktulga, R. Berger, D. S. Bolintineanu, W. M. Brown, P. S. Crozier, P. J. in 't Veld, A. Kohlmeyer, S. G. Moore, T. D. Nguyen, R. Shan, M. J. Stevens, J. Tranchida, C. Trott and S. J. Plimpton, Computer Physics Communications, 2022, **271**, 108171.
56 T. Schneider and E. Stoll, Physical Review B, 1978, **17**, 1302–1322.
57 H. J. C. Berendsen, J. P. M. Postma, W. F. van Gunsteren, A. DiNola and J. R. Haak, The Journal of Chemical Physics, 1984, **81**, 3684–3690.
58 L. J. Michot, I. Bihannic, K. Porsch, S. Maddi, C. Baravian, J. Mougel and P. Levitz, Langmuir, 2004, **20**, 10829–10837.
59 F. Hubert, L. Caner, A. Meunier and E. Ferrage, American Mineralogist, 2012, **97**, 384–398.
60 R. Eppenga and D. Frenkel, Molecular Physics, 1984, **52**, 1303–1334.
61 D. Tessier, in Soil Colloids and Their Associations in Aggregates, NATO ASI Series (Series B: Physics), ed. M. De Boodt, M. Hayes, A. Herbillon, E. De Strooper and J. Tuck, Springer, Boston, MA, 1990, pp. 387–415.
62 P. B. Malla, Clays and Clay Minerals, 1993, **41**, 412–422.
63 K. Mystkowski, J. . Środoń and F. Elsass, Clay Minerals, 2000, **35**, 545–557.
64 J.-F. Wagner, in Developments in Clay Science, Elsevier Ltd., 2nd edn., 2013, vol. 5, pp. 347–381.
65 W. Baille, S. Tripathy and T. Schanz, Applied Clay Science, 2010, **48**, 324–333.
66 L. Ye, Y. F. Jin, Q. Y. Zhu and P. P. Sun, Geotechnical Engineering Journal of the SEAGS & AGSSEA, 2015, **46**, 46–53.
67 J.-M. Fleureau, S. Kheirbek-Saoud, R. Soemitro and S. Taibi, Canadian Geotechnical Journal, 1993, **30**, 287–296.
68 B. Carrier, L. Wang, M. Vandamme, R. J.-M. Pellenq, M. Bornert, A. Tanguy and H. Van Damme, Langmuir, 2013, **29**, 12823–12833.
69 M. B. Pinson, E. Masoero, P. A. Bonnaud, H. Manzano, Q. Ji, S. Yip, J. J. Thomas, M. Z. Bazant, K. J. Van Vliet and H. M. Jennings, Physical Review Applied, 2015, **3**, 064009.
70 R. Moore, Géotechnique, 1991, **41**, 35–47.

Appendices

A Energy wells and barrier

The expressions of two minima E_1 and E_2 of the w-potential, and of the local maximum E_m in-between are:

$$\begin{cases} E_m = F_0\,(r_2 - r_1) \\ E_1 = \dfrac{3}{2}F_0\,(r_2 - r_1) - K_1\dfrac{(r_2 - r_1)^2}{8\left(1+\frac{K_1}{K_2}\right)} - \dfrac{(F_0)^2}{2}\left(\dfrac{1}{K_2}+\dfrac{1}{K_1}\right) \\ E_2 = \dfrac{1}{2}F_0\,(r_2 - r_1) - K_2\left(\dfrac{r_2 - r_1}{4}\right)^2 - \dfrac{(F_0)^2}{K_2} \end{cases} . \quad (7)$$

The two minima are of equal energy if the shifting force constant F_0 verifies :

$$F_0 = F_0^{eq} = \frac{K_1\left(r_2 - r_1\right)}{\frac{K_1}{K_2} - 1}\left(\frac{3\frac{K_1}{K_2}+1}{\sqrt{8\frac{K_1}{K_2}\left(\frac{K_1}{K_2}+1\right)}} - 1\right) \tag{8}$$

and the corresponding energy barrier separating the two minima is:

$$\Delta E = E_m - E_1 = E_m - E_2 = K_2\left(\frac{F_0^{eq}}{K_2} + \frac{r_2 - r_1}{4}\right)^2 \tag{9}$$

B Dimensionless formulation

A dimensionless formulation is used for practical implementation of the model. It is obtained by reducing Eqs. 1, 2 and 3 with respect to the length r_1 and to the moduli K_2 (unit of energy per square length). Dimensionless quantities are identified by symbol "$\sim$" over the quantity. The dimensionless formulation relates the reduced force $\tilde{F} = F/\left(K_2 r_1\right)$ and energy $\tilde{E} = E/\left(K_2 r_1^2\right)$ to the reduced distance $\tilde{r} = r/r_1$ and bond length $\tilde{l} = l/r_1$. Five reduced parameters are used: $\tilde{K}_1 = K_1/K_2$, $\delta\tilde{r} = \left(r_2 - r_1\right)/r_1$, $\tilde{K}_{angle} = K_{angle}/\left(K_2 r_1^2\right)$, $\tilde{K}_{bond} = K_{bond}/K_2$, and $\tilde{F}_0 = F_0/\left(K_2 r_1\right)$. A dimensionless simulation considers the reduced temperature $\tilde{T} = kT/\left(K_2 r_1^2\right)$, and yields the reduced pressure $\tilde{p} = p/K_2$. The dimensionless expression of the potential is:

$$\tilde{F}\left(\tilde{r}\right) = \begin{cases} \tilde{F}_0 - \tilde{K}_1\left(\tilde{r}-1\right) & \text{if } \tilde{r} \le 1 + \frac{\delta\tilde{r}}{2\left(1+\tilde{K}_1\right)} \\ \tilde{F}_0 + \left(\tilde{r} - \left(1 + \frac{\delta\tilde{r}}{2}\right)\right) & \text{if } 1 + \frac{\delta\tilde{r}}{2\left(1+\tilde{K}_1\right)} \le \tilde{r} \le 1 + \frac{3\delta\tilde{r}}{4} \\ \tilde{F}_0 - \left(\tilde{r} - \left(1 + \delta\tilde{r}\right)\right) & \text{if } 1 + \frac{3\delta\tilde{r}}{4} \le \tilde{r} \le 1 + \frac{5\delta\tilde{r}}{4} \\ \tilde{F}_0 + \left(\tilde{r} - \left(1 + \frac{3\delta\tilde{r}}{2}\right)\right) & \text{if } 1 + \frac{5\delta\tilde{r}}{4} \le \tilde{r} \le -\tilde{F}_0 + 1 + \frac{3\delta\tilde{r}}{2} \\ 0 & \text{if } -\tilde{F}_0 + 1 + \frac{3\delta\tilde{r}}{2} \le \tilde{r} \end{cases} \tag{10}$$

$$\tilde{E}\left(\tilde{r}\right) = \begin{cases} -\tilde{F}_0\left(\tilde{r} - \left(1 + \frac{3\delta\tilde{r}}{2}\right)\right) + \frac{1}{2}\tilde{K}_1\left(\tilde{r}-1\right)^2 - \tilde{K}_1\frac{\left(\delta\tilde{r}\right)^2}{8\left(1+\tilde{K}_1\right)} - \frac{\left(\tilde{F}_0\right)^2}{2} \\ \qquad \text{if } \tilde{r} \le 1 + \frac{\delta\tilde{r}}{2\left(1+\tilde{K}_1\right)} \\ -\tilde{F}_0\left(\tilde{r} - \left(1 + \frac{3\delta\tilde{r}}{2}\right)\right) - \frac{1}{2}\left(\tilde{r} - \left(1 + \frac{\delta\tilde{r}}{2}\right)\right)^2 - \frac{\left(\tilde{F}_0\right)^2}{2} \\ \qquad \text{if } 1 + \frac{\delta\tilde{r}}{2\left(1+\tilde{K}_1\right)} \le \tilde{r} \le 1 + \frac{3\delta\tilde{r}}{4} \\ -\tilde{F}_0\left(\tilde{r} - \left(1 + \frac{3\delta\tilde{r}}{2}\right)\right) + \frac{1}{2}\left(\tilde{r} - \left(1 + \delta\tilde{r}\right)\right)^2 - \left(\frac{\delta\tilde{r}}{4}\right)^2 - \frac{\left(\tilde{F}_0\right)^2}{2} \\ \qquad \text{if } 1 + \frac{3\delta\tilde{r}}{4} \le \tilde{r} \le 1 + \frac{5\delta\tilde{r}}{4} \\ -\tilde{F}_0\left(\tilde{r} - \left(1 + \frac{3\delta\tilde{r}}{2}\right)\right) - \frac{1}{2}\left(\tilde{r} - \left(1 + \frac{3\delta\tilde{r}}{2}\right)\right)^2 - \frac{\left(\tilde{F}_0\right)^2}{2} \\ \qquad \text{if } 1 + \frac{5\delta\tilde{r}}{4} \le \tilde{r} \le -\tilde{F}_0 + 1 + \frac{3\delta\tilde{r}}{2} \\ 0 \qquad \text{if } -\tilde{F}_0 + 1 + \frac{3\delta\tilde{r}}{2} \le \tilde{r} \end{cases} \tag{11}$$

$$\begin{cases} \tilde{E}_{angle}(\theta) = \tilde{K}_{angle}\left(\theta - \theta_0\right)^2 \\ \tilde{E}_{bond}(\tilde{l}) = \tilde{K}_{bond}\left(\tilde{l} - \tilde{l}_0\right)^2 \end{cases} \tag{12}$$

C Derivation of intra-layer parameters

In this section, we provide the expressions of the intra-layer harmonic parameters K_{angle} and K_{bond} in function of the longitudinal and bending stiffnesses of a single clay mineral layer, respectively. These stiffnesses have been estimated by molecular simulation by Honorio et al.[51] for Na-Mnt. The expressions are obtained through correspondence of energy between a continuous plate and the discrete chain of particles.

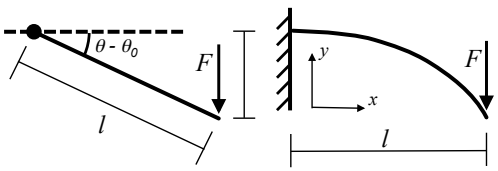

Fig. 19 Equivalent situation implemented by the angle potential (on the left) to a cantilever load at its end (one the right).

Let us consider a thin cantilever plate of length l_0 loaded by a transverse force F at its end, as illustrated in Fig. 19 (right). Applying the usual thin plate theory (Kirchhoff-Love), the transverse displacement at the point of application of the force is $\delta = \frac{l_0^3 F}{3D}$, with D the bending stiffness of the plate (e.g., $D = \frac{Eh_0^3}{12(1-\nu^2)}$ for a plate of thickness h_0 made of a homogeneous isotropic material of Young's modulus E and Poisson's ratio ν). Thanks to the linearity of the behavior, the mechanical work is quadratic with respect to the loading, which makes it possible to make a correspondence with the harmonic angle potential of the chain of particles. The energy per unit depth of the system takes the form :

$$E_{bending} = \frac{3D\delta^2}{l_0^3} \tag{13}$$

The equivalent configuration of a chain of particle is the contribution of a single angle (see Fig. 19, left) which corresponds to both a length and a depth of L_0, i.e., $E_{bending} l_0 = E_{angle}$ with $\left(\theta - \theta_0\right) \approx sin\left(\theta - \theta_0\right) = \delta/l_0$ (we assume small bending: $\theta - \theta_0 \ll 1$). Therefore, we can identify the angle harmonic coefficient as:

$$K_{angle} = 3D \tag{14}$$

Likewise, let us consider a thin cantilever plate submitted to an elongation force at its free boundary. The energy per unit depth of the system is

$$E_{elongation} = \frac{A}{l_0}\left(l - l_0\right)^2 \tag{15}$$

with A the elongation stiffness of the plate ($A = \frac{Eh_0}{1-\nu^2}$ for a plate of thickness h_0 made of a homogeneous isotropic material). Again the quadratic form of the energy makes it possible to ensure a correspondence with the harmonic bond energy of the chain of particles, i.e., $E_{elongation} l_0 = E_{bond}$. We obtain :

$$K_{bond} = A \tag{16}$$

We considering the stiffnesses estimated by Honorio et al.[51] for Na-Mnt: $D \approx 2 \cdot 10^{-17}$ N.m and $A \approx 240$ N/m. Substituting into eq. 14 and 16 provides the following estimations of the intra-layer harmonic parameters:

$$\begin{cases} K_{angle} = 6 \times 10^{-17} \text{ N.m} \\ K_{bond} = 240 \text{ N/m} \end{cases} \tag{17}$$

D Strain rate effect

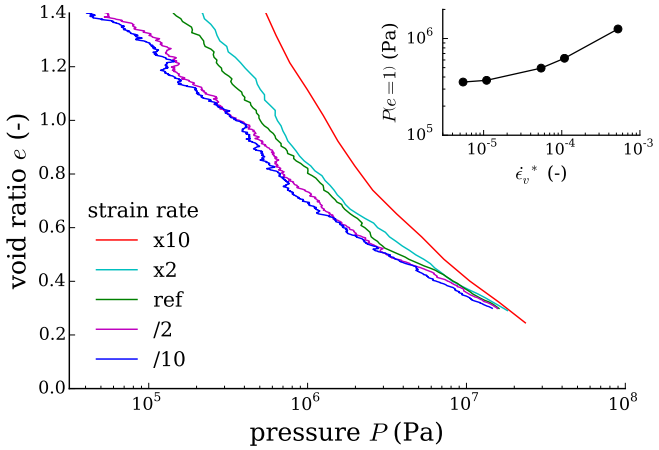

Fig. 20 Effect of the considered engineering strain rate on the mechanical response to isotropic compression. The reference rate corresponds to $\dot{\varepsilon}_v^* = \dot{\varepsilon}_v \sqrt{m/K_2} = 6.52 \cdot 10^{-5}$. The inset displays the pressure at a void ratio $e = 1$ as a function of the strain rate.